Towards precise prediction of transport properties from synthetic computer tomography of reconstructed porous media

B. Biswal,[1,2] R. J. Held,[3] V. Khanna,[1] J. Wang,[1] and R. Hilfer[1,4]
[1]*ICP, Universität Stuttgart, Pfaffenwaldring 27, 70569 Stuttgart, Germany*
[2]*S. V. College, University of Delhi, New Delhi 110 021, India*
[3]*StatoilHydro ASA, N-7005 Trondheim, Norway*
[4]*Institut für Physik, Universität Mainz, 55099 Mainz, Germany*
(Received 4 April 2009; published 2 October 2009)

Transport properties of a multiscale carbonate rock are predicted from pore scale models, reconstructed using a continuum geometrical modeling technique. The method combines crystallite information from two-dimensional high-resolution images with sedimentary correlations from a three-dimensional low-resolution microcomputed tomography (μ-CT) image to produce a rock sample with calibrated porosity, structural correlation, and transport properties at arbitrary resolutions. Synthetic μ-CT images of the reconstructed model match well with experimental μ-CT images at different resolutions, making it possible to predict physical transport parameters at higher resolutions.

DOI: 10.1103/PhysRevE.80.041301 PACS number(s): 81.05.Rm, 02.70.−c, 47.56.+r, 91.60.Np

I. INTRODUCTION

The prediction of macroscopic petrophysical transport parameters from the microstructure of porous media remains a focus of research in physics and engineering [1–5]. Pore scale research requires reasonably accurate three-dimensional microscopic images of the rock as input [6,7]. Although μ-CT images are normally used for this purpose, this experimental technique is expensive and can be inadequate due to lack of sufficient resolution or sampling volume. To overcome these restrictions a number of computational modeling techniques have been proposed to reconstruct the microscopic digital images of porous media computationally [8–13]. Most of these methods try to directly incorporate statistical properties such as porosity and correlation functions computed from thin-section images into binary three-dimensional grid representations of the underlying rock [14–17]. Methods using thresholded Gaussian fields [8,18–20] and simulated annealing [9,21,22] have been particularly successful in this effort. Process-oriented methods attempt to reproduce the relevant physicochemical diagenetic processes [23–25].

A major shortcoming of these methods has been the emphasis on a representative grid at a specific resolution. Petrophysical parameters in multiscale porous media such as carbonates and clay filled sandstones depend strongly on resolution. In the multiscale carbonate rock analyzed and modeled in this work, the smallest calcite-dolomite crystallite sizes are between 1 to 10 μm. One requires at least a resolution of 10 nm (sidelength of the voxel) to resolve them [26]. Thus, even a small cubic sample of sidelength 10^4 μm requires a minimum $10^6 \times 10^6 \times 10^6$ grid representation, i.e., 10^{18} numbers. Typical experimental plugs have diameters in the range of 1.5–3.5 cm and cannot be modeled with such a modeling approach. There appears to be no hope that mere increase in resolution in experimental μ-CT imaging can provide tomograms for multiscale carbonates. Recent efforts on inferring subresolution microporosity from μ-CT images of carbonate rock, thereby predicting petrophysical transport properties at higher resolutions, point out current shortcomings [27,28]. In this paper we overcome such limitation by generating a computer model for carbonate rock based on a continuum approach [13].

The carbonate rock modeled is a fully dolomitized oolithic grainstone [29]. We reconstruct the pore scale representation of a cubic section (sidelength approx. 4.22 mm) of the rock. The model parameters are calibrated to match quantitatively the morphology, porosity, two-point correlation function, etc. between the synthetic μ-CT image from the model and the experimental μ-CT image at a specific resolution. Having achieved this, physical transport parameters are then computed at intermediate and higher resolutions from synthetic μ-CT images of the model.

The paper is organized as follows. The problem is formulated in Sec. II. For completeness a brief description of the model is presented in Sec. III. In Sec. IV the quantitative image analysis used to determine the model parameters is described. Section V describes the method of incorporating structural correlation from a low-resolution μ-CT image. The computational implementation is described in Sec. VI. Quantitative microstructure comparisons at a specific resolution are given in Sec. VIII. The predicted transport properties of the sample at higher resolutions are presented in Sec. IX.

II. FORMULATION OF THE PROBLEM

The aim of this work is to present a method to generate large (laboratory scale) volumes of a multiscale rock microstructure from partial resolution information. The model is then used to successfully predict physical transport parameters at higher resolutions where μ-CT imaging is either not available or not possible.

More specifically, based on the information gathered from the thin-section image of the rock shown in Fig. 1, from the two-dimensional high-resolution microscopic images shown in Fig. 2 and from the three-dimensional poor resolution μ-CT image shown in Fig. 4, we aim to reconstruct an accurate three-dimensional continuum representation of a suf-

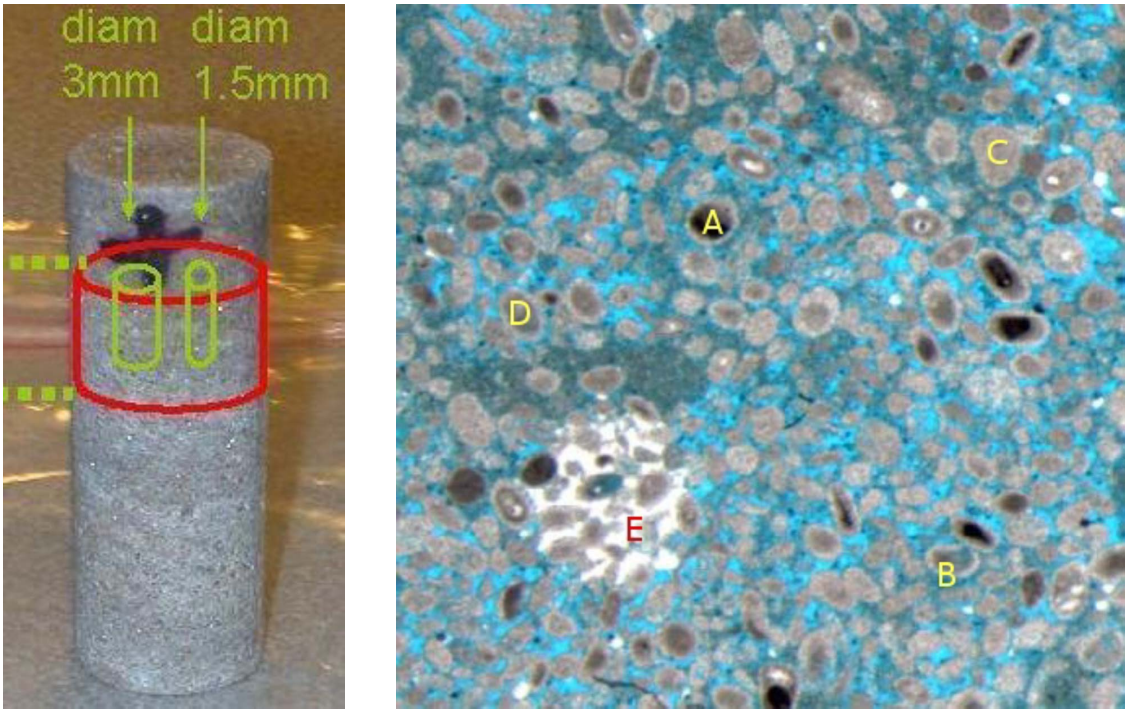

FIG. 1. (Color online) Left: image of a core plug (diameter=1.5 cm) showing the subsampling procedure for experimental microcomputer tomography. Right: a thin-section image from a section of the modeled carbonate rock. The resolution of this optical scan is 4.6 μm per pixel. The size of the image shown is 2.065 mm $\times$ 1.996 mm. Pore space is impregnated blue (medium gray). The label A indicates a vuggy pore region. The labels B (oolithic rim), C (densely packed ooid core), D (loosely packed ooid core), and E (cement) indicate regions with distinct crystallite properties.

ficiently large carbonate rock sample. The main steps are summarized below.

First, the modeling procedure requires information on the type of crystallites, their size, overlap, orientation, and density of packing. These model parameters can be extracted from high-resolution two-dimensional images. For any specific rock such microscopic images can be easily obtained. In the current work the regions with distinct crystallite properties are first determined from the thin-section image shown in Fig. 1. The type, shape, size, overlap, and orientation of the crystallites in each of these separate regions are determined from higher magnification scanning electron microscope (SEM) images of the rock shown in Fig. 2.

Second, reconstruction of a realistic rock microstructure must incorporate sedimentary textural correlations visible in the original rock at many scales. The question of how to reproduce such multiscale correlations was addressed and solved in Refs. [12,13]. It involves construction of a three-dimensional primordial filter function G (details in Secs. III and V). In this work G is constructed from a poor resolution μ-CT image. As shown in Fig. 4, this low-resolution image hardly resolves the microporosity (intercrystalline pore space below the resolution of the μ-CT image) or any of the dolomite crystallites. As a result, this image is not suitable for estimating accurate physical and transport properties for this rock. We show that such a μ-CT image is yet suitable for generating G, and combined with the information obtained from two-dimensional images, is sufficient to construct a realistic model. Most importantly, such low-resolution images are of large size allowing us to generate laboratory scale models. The continuum nature of the model provides a microstructure representation of the rock at arbitrary resolutions, making it possible to predict petrophysical parameters at higher resolutions.

III. MODEL

In this model [12,13], the rock occupying a bounded region $\mathbb{S} \subset \mathbb{R}^3$ is represented by crystallites placed in the continuum. The model belongs to a class of models in stochastic geometry known as germ-grain models [30]. Based on the depositional texture of the given rock, $\mathbb{S}$ is first divided into a number of different regions, each corresponding to distinct crystallite properties such as type, size, overlap, and orientation distribution. Crystallites for each of these regions are deposited separately in a random sequence and then combined. Each element

$$\omega_i = (\mathbf{x}_i, R_i, \mathbf{a}_i, T_i) \tag{1}$$

of the sequence represents a crystallite of type T_i at spatial position $\mathbf{x}_i \in \mathbb{S}$ with inscribed sphere radius R_i and orientation $\mathbf{a}_i$.

Multiscale porous media, such as many carbonates, do not contain a purely random geometry. Often, primordial depositional textures, such as the structure of the original ooids or bioclasts are visible in the final geometry [29,31]. For ex-

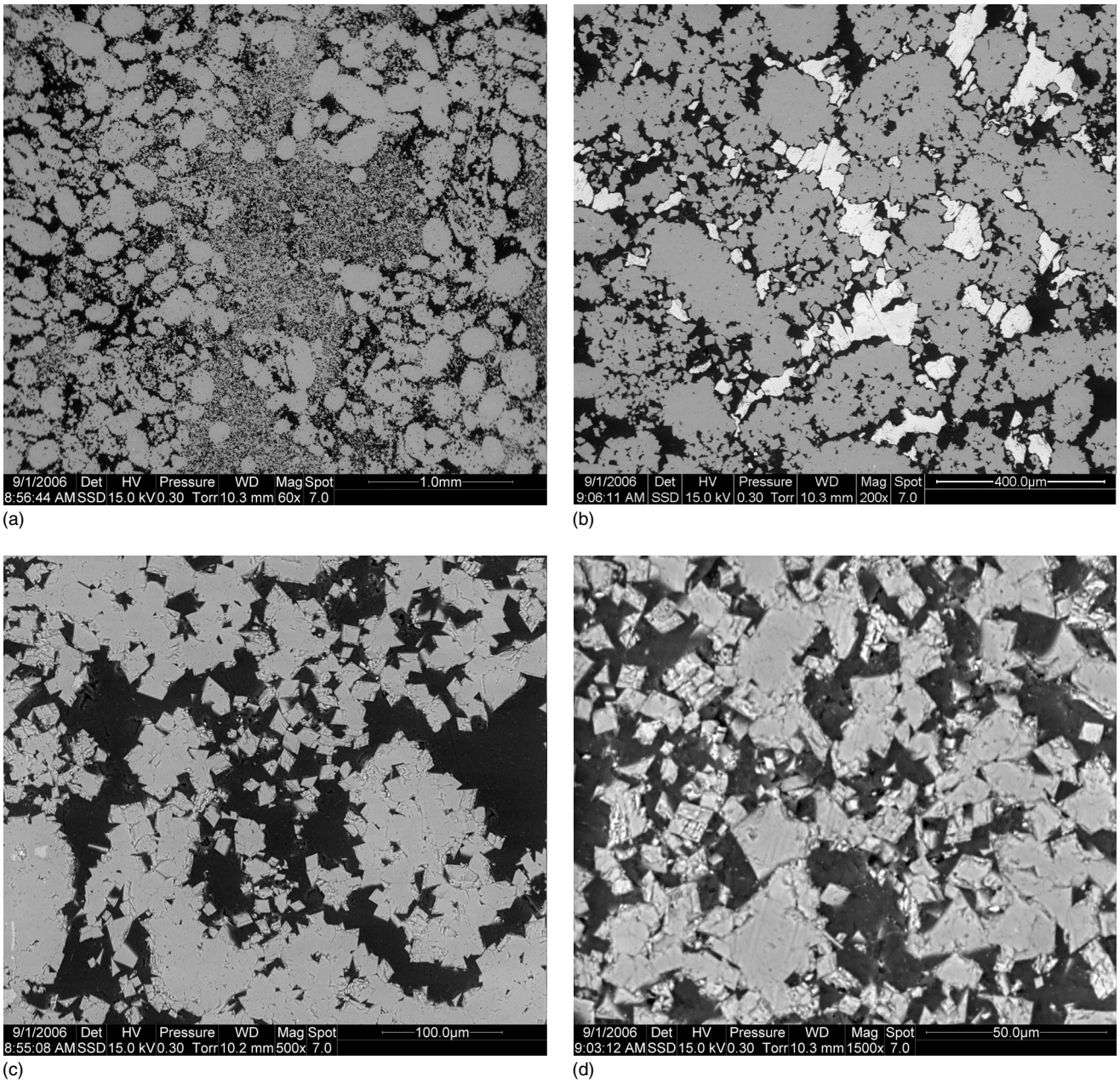

FIG. 2. Scanning electron microscope images of the modeled carbonate rock at different magnifications (top left: 3.8 mm $\times$ 3.28 mm at 60$\times$ magnification and 1.06 μm/pixel. Top right: 1.292 mm $\times$ 1.117 mm at 200$\times$ magnification and 1.26 μm/pixel. Bottom left: 455 μm $\times$ 392 μm at 500$\times$ magnification and 126 nm/pixel. Bottom right: 151 μm $\times$ 131 μm at 1500$\times$ magnification and 42 nm/pixel). The crystallite types, sizes, and overlap are determined from these images.

ample, the thin-section image of the rock modeled in this work (Fig. 1) shows the shape of the original ooids before the dolomitization, although these ooids are now fully dolomitized into many small dolomite crystallites as seen in the magnified images (Fig. 2).

In modeling of such rocks, the attributes of the crystallites defining the rock in the continuum need to be correlated with the primordial depositional texture of the rock. This is done by defining a grayscale primordial filter function $G:\mathbb{S} \rightarrow [0,1]$ that is carefully constructed from the images and geological information available on the rock. $G(\mathbf{x})$ is a given function that determines whether a crystallite can be deposited at $\mathbf{x}$ and of what size, orientation, type, etc. The crystallite attributes are defined through G as

$$R_i = \mathcal{R}(G(\mathbf{x}_i)), \quad \mathbf{a}_i = \mathcal{A}(G(\mathbf{x}_i)), \quad T_i = \mathcal{T}(G(\mathbf{x}_i)), \qquad (2)$$

where $\mathcal{R}:[0,1] \rightarrow [R_{\min}, R_{\max}] \cup \{0\}$, $\mathcal{A}:[0,1] \rightarrow \mathbb{E}$, and $\mathcal{T}:[0,1] \rightarrow \{1,2,\ldots,g\}$. $\mathbb{E}=\{\mathbf{x} \in \mathbb{R}^3 : |\mathbf{x}|=1\}$ is the unit sphere, $[R_{\min}, R_{\max}] \subset \mathbb{R}^1$ and g is the number of separate regions within the rock with distinct crystallite properties. If $\mathbf{x}_i$ falls in the pore space (including the vuggy pores), $\mathcal{R}(G(\mathbf{x}_i))=0$, and no crystallite deposition is allowed there.

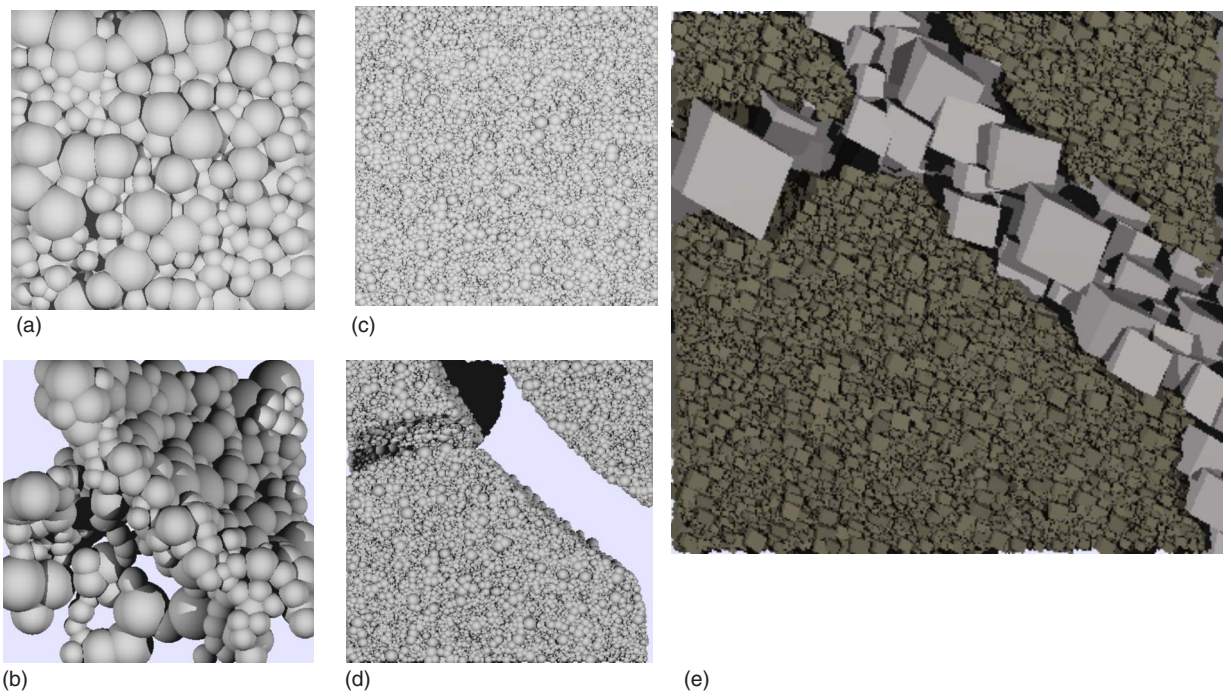

FIG. 3. (Color online) A schematic representation of the continuum modeling technique for an imaginary carbonate rock texture that contains two separate regions with distinct crystallite properties. The overlapping spheres deposited separately for each region are shown in (a) and (c). These are filtered through G in (b) and (d), respectively. The combined list is then decorated with dolomite crystallites in (e).

To ensure a fully supported matrix, each deposited crystallite must have a finite overlap with at least one of the existing deposits. However, the crystallites can have complex geometry and computation of the overlap between them may not be possible always. In the following model implementation, the overlap is computed indirectly by associating a spherical radius R_i to each chosen point $\mathbf{x}_i$ and ensuring that the degree of overlap with any adjacent sphere at $\mathbf{x}_j$ as computed by

$$O(\omega_i,\omega_j)=\frac{R_i+R_j-|\mathbf{x}_i-\mathbf{x}_j|}{R_i+R_j-|R_i-R_j|} \tag{3}$$

is finite and smaller than $\lambda_i=\Lambda(G(\mathbf{x}_i))$. This new function $\Lambda:[0,1]\rightarrow[\lambda_{\min},\lambda_{\max}]$ also correlates the degree of crystallite overlap with the primordial depositional texture through G.

The porosity of the crystallite packing in each region, thereby the porosity of the final sample, is controlled by depositing points in each region with a specific point density ρ_j, $j=1,2,\ldots,g$.

To summarize, a separate list of points are deposited in $\mathbb{S}$ for each region with distinct crystallite properties and then combined to form the list of N objects that represents the rock in the continuum. Each of these distinct regions corresponds to a well defined grayscale interval in the primordial filter function G. The deposited points are then decorated with geometric objects defining the crystallite type T_i, size $d_i(R_i)$, and orientation $\mathbf{a}_i$.

The rock sample is fully represented by a list of N quadruples $(\mathbf{x}_i,d_i,\mathbf{a}_i,T_i)$. In Eq. (3), R_i is the radius of the sphere associated with the point at $\mathbf{x}_i$. Therefore, the size of the crystallite $d_i(R_i)$ must appropriately scale with R_i so as to retain the matrix connectivity. Because the deposited spheres are inscribed in the crystallites, this condition is implicitly fulfilled in this model implementation.

A schematic representation of a model implementation for a generic carbonate rock with two separate regions of distinct crystallite properties is shown in Fig. 3. The depositions of points with associated overlapping spheres with different $[R_{\min},R_{\max}]$ for each region are shown in Figs. 3(a) and 3(b). In Figs. 3(c) and 3(d) these two lists are separately filtered through the primordial filter function G. Only the points allowed in the respective regions are retained and others removed. The lists are then combined and decorated with dolomite type crystallites (rhombohedra) as shown in Fig. 3(e).

IV. IMAGE ANALYSIS AND MODEL PARAMETERS

For each region of the modeled rock with distinct crystallite properties, the model parameters needed for the reconstruction are the following: the type of crystallite (T), the minimum and maximum radii of the inscribed spheres $(R_{\min},R_{\max})$, the minimum and maximum allowed overlap between the inscribed spheres $(\lambda_{\min},\lambda_{\max})$, and the number density of the crystallites ρ. These parameters, the primordial filter function G, and the functions defined in Eq. (2) are to be determined from the available information on the rock microstructure. It can be a combination of geological information available on the rock, image analysis of two-dimensional micrographs, thin-section analysis, SEM images, and three-dimensional μ-CT images.

The number of separate regions with distinct crystallite properties is determined from the high-resolution thin-

TABLE I. Model parameters for separate regions with distinct crystallite properties used for the modeling of the carbonate rock sample.

Region	Description	R_{min} (μm)	R_{max} (μm)	λ_{max}	ρ
I	Oolithic rim	6	10	0.3	1.5×10^{-3}
II	Ooid core (dense)	4	10	0.4	2.5×10^{-3}
III	Ooid core (loose)	4	10	0.2	1.5×10^{-3}
IV	Cement	5	10	0.8	1.0×10^{-2}

section microscopic image of the rock shown in Fig. 1. The outlines of the fully dolomitized ellipsoidal ooids (grains) are clearly visible. There are three kinds of pore space observed: vugs (marked A in Fig. 1), macroporosity in the form of intergrain pore space (between the grains), and microporosity in the form of intragrain pore space (within the primordial grains and between the crystallites). The four different regions are the oolithic rims or the isopachous layer around each grain (marked B in Fig. 1), grains with densely packed crystallites in the core (marked C in Fig. 1), grains with loosely packed crystallites in the core (marked D in Fig. 1), intergrain euhedral dolomite crystallites and cement (marked E in Fig. 1).

The crystallite types, sizes, and their overlap in each region are estimated from the SEM images of surface sections available at different magnifications. These are shown in Fig. 2. The values of the model parameters R_{min} and R_{max} for each region are measured manually from these images and presented in Table I. The crystallites in each region are equilateral rhombohedra (dolomite) and of the same shape. The shapes of the crystallites in the cement region are not visible. This region is also modeled with dolomites with high overlap to achieve zero porosity. The geometric definition of the dolomite type crystals (rhombohedra) is presented in Eq. (4). The minimum overlap λ_{min} is set to zero as many crystallites appear to touch each other. The maximum overlap λ_{max} and the point density ρ are difficult to measure accurately from these two-dimensional images. Initial estimates, as starting values, are chosen from the visual inspection of these images and then calibrated later to match the microstructure quantitatively (described in the Sec. VI). The final model parameters after the calibration are summarized in Table I. Note that the two-dimensional images shown in Figs. 1 and 2 are sufficient to determine the model parameters for this rock.

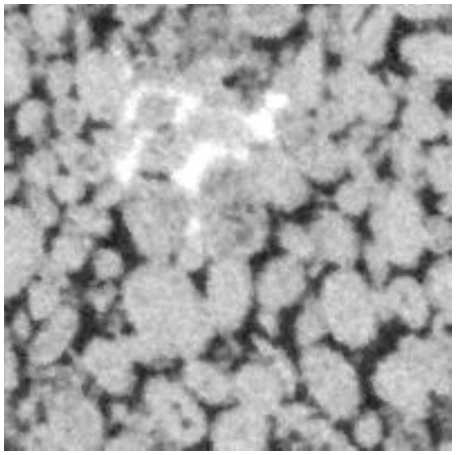

FIG. 4. A 200×200 cross section of the experimental μ-CT image at resolution 8.06 μm. At this resolution only the ooid shapes are resolved and no clear dolomite shape is visible. A 524^3 section from the three-dimensional μ-CT image at this resolution is used for generating the filter function $G(\mathbf{x})$.

V. GENERATION OF $G(\mathbf{x})$

One of the main components of the modeling procedure outlined in Sec. III is the construction of a primordial filter function G. Through this reference function the correlation with the depositional texture of the original rock is built into the model. The type of a crystallite, its size, orientation, and overlap at any point are determined from G through the functions in Eq. (2).

We have used the μ-CT image at the resolution of 8.06 μm for constructing $G(\mathbf{x})$. The original grayscale μ-CT image, a section of which is shown in Fig. 4, is processed and converted to a segmented images as shown in Fig. 5 and described in the next paragraph. This segmented image represents $G(\mathbf{x})$. Separate grayscale values in this image corre-

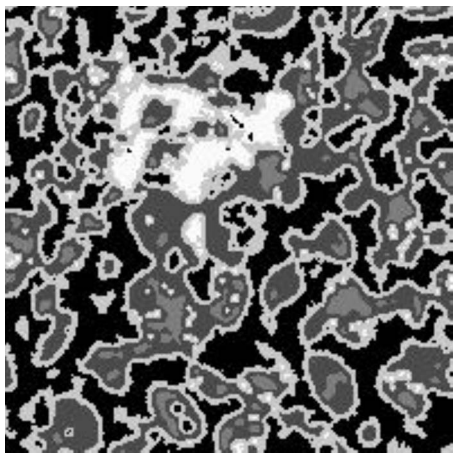

FIG. 5. Grayscale representation of $G(\mathbf{x})$. White voxels represent the anhydride cement region and black voxels represent the pore space. The oolithic rim region is marked by light gray, the region with densely packed crystallites is marked by dark gray, and the region with loosely packed crystallites is marked by medium gray.

spond to separate regions with distinct crystallite properties (Table I).

To construct Fig. 5 from Fig. 4, a 524^3 grid of the μ-CT image at the resolution of 8.06 μm is filtered using the Hybrid 3D Median Filter in the public domain image analysis software IMAGEJ [32,33]. The filter is applied for reducing the noise level. Being an 8-bit image, the 524^3 voxels have grayscale values between 0–255. A threshold value of 154 is chosen to identify the space where no crystallite will be deposited. This volume, with a volume fraction of 0.3581, includes the intergrain pore space and the vuggy pores. Although no crystallites are deposited in this volume, it is not entirely pore space. This is because some of the crystallites placed outside this volume will protrude into this volume. A new grayscale value of 0 is assigned to the voxels having grayscale values below this threshold. These voxels are shown in black in Fig. 5. A threshold value of 215 is chosen to identify the voxels that represent the cement region. The volume fraction of the cement region is 0.0167. A grayscale value of 255 is assigned to the voxels having grayscale values above this threshold. These are shown in white in Fig. 5.

The remaining voxels represent the three remaining regions: oolithic rim, densely packed ooid core, and loosely packed ooid cores. The 524^3 grayscale grid is then smoothed recursively (in IMAGEJ) until a smooth grayscale image is obtained for the matrix region without altering the voxels having the grayscale value of 0 or 255. The grayscale intervals for different regions are then determined by careful comparison with the thin-section image shown in Fig. 1. These are 1–157 for the isopachous rim (volume fraction 0.3063), 158–213 for the densely packed ooid cores (volume fraction 0.2499), and 214–254 for loosely packed ooid cores (volume fraction 0.0689). In the final segmented image shown in Fig. 5 these regions are marked by grayscale values of 200 (light gray), 75 (dark gray), and 125 (medium gray), respectively.

VI. MODEL IMPLEMENTATION

The model implementation follows the procedure outlined in Ref. [13]. The reconstructed cubic carbonate rock volume has a sidelength of $\ell=4.2234$ mm. To eliminate boundary effects, we chose a cubic sample $\mathbb{S}$ of sidelength $\ell=4.1267$ mm from the center of this volume for final analysis. This corresponds to a 512^3 voxel representation at 8.06 μm resolution. A model is generated with the model parameters assessed from the image analysis (Sec. IV), then discretized at resolution 8.06 μm (Sec. VII) and its microstructure is compared with the original experimental μ-CT image at resolution 8.06 μm (Sec. VIII). The model parameters ρ and $\lambda_{\max}$ are then calibrated so that the discretization of the model at resolution 8.06 μm matches closely with the original μ-CT image at this resolution. The model parameters summarized in Table I are the final calibrated parameters. The analysis presented in Sec. VIII and the physical parameters computed in Sec. IX are based on the model generated with these final calibrated model parameters.

The continuum list representing $\mathbb{S}$ contains millions of crystallites. The deposition rule requires a computational scheme for random deposition of overlapping polydisperse spheres in $\mathbb{S}$. These are deposited separately for each region and combined to form the final list. In region j, randomly chosen points $\mathbf{x}_i$ are added to the list if both $G(\mathbf{x}_i) \in [G^j_{\min}, G^j_{\max}]$ and Eq. (3) are satisfied simultaneously. $[G^j_{\min}, G^j_{\max}]$ is the grayscale interval in G that corresponds to the region j. For computational efficiency we divide $\mathbb{S} \subset \mathbb{R}^3$ into smaller overlapping cubic cells $\mathbb{U}$, i.e., $\mathbb{S} = \mathbb{U}_1 \cup \mathbb{U}_2 \cup \mathbb{U}_3 \ldots$. Points are deposited randomly in each cell $\mathbb{U}_i$ and added to the final list. This scheme provides fast convergence in the deposition as Eq. (3) is verified only for a small set of existing points in $\mathbb{U}_i$ and the neighboring cells. To prevent correlation from the cubic cell division entering into the deposition scheme, the size of the cells and overlap between neighboring cells are kept large, and the cells are filled in a random sequence.

Each point in the list is then decorated by dolomites. These are equilateral rhombohedra and each rhombohedron $\mathbb{G}_i$ (before rotation) centered at $\mathbf{x}_i$ is defined by the intersection of three pairs of parallel planes. Each pair is separated by a distance d_i and tilted by an angle of α degrees about the coordinate axes to which they are parallel initially. The equations of these three pairs of planes are

$$\mathbf{n}_j \cdot \mathbf{x} \pm \frac{d_i}{2} = 0, \quad j = 1,2,3, \tag{4}$$

where $\mathbf{n}_1=(\cos\alpha, 0, -\sin\alpha)$, $\mathbf{n}_2=(-\sin\alpha, \cos\alpha, 0)$, and $\mathbf{n}_3=(0, -\sin\alpha, \cos\alpha)$. For this carbonate rock the dolomite rhombohedra in all regions appear similar in shape. We have assumed $\alpha=-15$ deg to define the rhombohedra.

The orientations of the crystallites are represented through generalized quaternions. For a dolomite $\mathbb{G}_i$, with the origin of the coordinate system at $\mathbf{x}_i$, the orientation $\mathbf{a}_i$ is defined by a sequence of three rotations of θ_1, θ_2, and θ_3 about the coordinate axes $\mathbf{e}_1=(1,0,0)$, $\mathbf{e}_2=(0,1,0)$, and $\mathbf{e}_3=(0,0,1)$, respectively, thus

$$\mathbf{a}_i = \mathcal{A}(G(\mathbf{x}_i)) = \mathcal{Q}_{i3}\mathcal{Q}_{i2}\mathcal{Q}_{i1}, \tag{5}$$

where the unit quaternion $\mathcal{Q}_{ij}$ represents a rotation of θ_j about the vector $\mathbf{e}_j$. The orientations of crystallites appear random in each region. From the image analysis the rotation angle θ_j is chosen randomly from $[-60, 60]$ degrees. The rotation angles of the dolomites are estimated from the visual inspection of 2D images. The rotations are assumed isotropic and the same range is assumed in the z direction. The estimated parameters are accepted because it resulted in a qualitative match of the morphology at high resolutions. Roughly 5.15×10^7 rhombohedral crystallites represent the modeled rock sample.

For the discretization of the model described in the next section we need to determine if a point in the continuum falls inside any of the dolomite crystallites. A given point $\mathbf{p}$ falls into $\mathbb{G}_i$ if

$$\left(\mathbf{n}_j \cdot \mathbf{p}'_r + \frac{d_i}{2}\right)\left(\mathbf{n}_j \cdot \mathbf{p}'_r - \frac{d_i}{2}\right) < 0, \quad j = 1,2,3, \tag{6}$$

where $\mathbf{p}'_r = \mathbf{q}_i^{-1}(\mathbf{p}-\mathbf{x}_i)(\mathbf{q}_i^{-1})^*$ and $(.)^*$ is the quaternion conjugation.

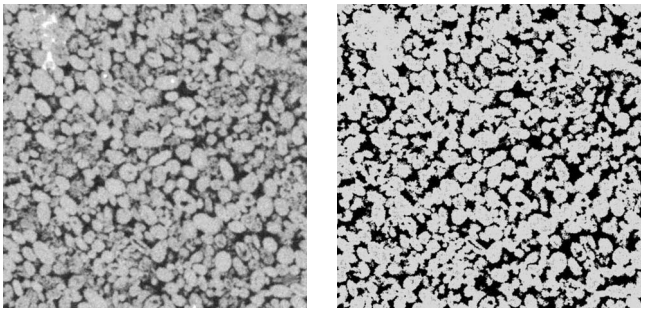

(a) (b)

FIG. 6. 512×512 cross section of the experimental μ-CT image (a) of the carbonate rock at the resolution 8.06 μm is compared with a matching cross section from the synthetic μ-CT image (b) of the model at this resolution.

VII. SYNTHETIC COMPUTER TOMOGRAPHY

The continuum representation allows discretization of the sample at arbitrary resolutions. The sample $\mathbb{S}$ is subdivided into a grid of cubic voxels, each of sidelength a. In each voxel n^3 collocation points ($n\times n\times n$ cubic sublattice) are positioned centrally. Each voxel is then labeled by a grayscale value $0\leq m\leq n^3$, where m is the number of collocation points that fall inside the deposited crystallites. Thus, a voxel with label (i) $m=n^3$ represents matrix because all the n^3 collocation points fall inside the matrix, (ii) $m=0$ represents pore because all the n^3 collocation points fall outside the matrix, and (iii) $0<m<n^3$ represents a voxel containing both pore and matrix because only a fraction of the n^3 collocation points fall inside the matrix.

This produces a grayscale image where the voxel label is the grayscale value of the voxel in the resulting image. This grayscale grid represents a synthetic μ-CT image of the computer model of the rock. The grayscale representation is analogous to the experimental μ-CT image that reflects the matrix density at each voxel. This synthetic μ-CT image can be used for comparison with experimental μ-CT images, microstructure analysis, parameter estimation, flow simulation, etc.

VIII. MICROSTRUCTURE ANALYSIS

The sample $\mathbb{S}$ is discretized at various resolutions. The discretization at resolution 8.06 μm is made to compare with the μ-CT image at the same resolution. The morphology of the model matches accurately with the original rock as seen from the comparison of the images in Fig. 6. Discretizations at lower and higher resolutions are also carried out for predicting porosity and permeability at intermediate and higher resolutions. This analysis is presented in Sec. IX.

These grayscale images are thresholded by the Otsu method [34] in IMAGEJ to obtain digitized representations. The μ-CT images are also digitized by the same method. There is no specific reason to chose this particular segmentation method, other than to choose *a priori* a segmentation method for converting the μ-CT images to binary image and the same method should be used for thresholding the synthetic μ-CT images.

The model implementation is done with G derived from the μ-CT image at the resolution 8.06 μm. A rigorous comparison of the microstructure between the digitized representation of the model and the experimental μ-CT image is first carried out at this resolution. This section is devoted to these quantitative microstructure measurements and comparison.

In the following, $\mathbb{S}\subset\mathbb{R}^3$ represents a discretized and segmented (=thresholded) sample (binary voxels placed in a simple cubic lattice) whose sidelength is M in units of the lattice constant a, the resolution of the discretization process. The two-component porous sample $\mathbb{S}=\mathbb{P}\cup\mathbb{M}$ is the union of two closed subsets $\mathbb{P}\subset\mathbb{R}^3$ and $\mathbb{M}\subset\mathbb{R}^3$, where $\mathbb{P}$ denotes the pore space and $\mathbb{M}$ denotes the matrix space. The characteristic (or indicator) function $\chi_{\mathbb{P}}(\mathbf{x})$ of the set $\mathbb{P}$ is defined as

$$\chi_{\mathbb{P}}(\mathbf{x})=\begin{cases}1 & \text{for } \mathbf{x}\in\mathbb{P}\\ 0 & \text{for } \mathbf{x}\notin\mathbb{P},\end{cases} \tag{7}$$

where $\mathbf{x}$ is the position vector of the voxel on the digitized grid.

A. Minkowski functionals

To ascertain the quality of the reconstructed model a quantitative comparison of the morphology is carried out based on the four Minkowski functionals [35,36]. Definitions of these widely used morphological measures from mathematical morphology are summarized in the Appendix. The method of computation from digitized images is described in Ref. [37]. The computed Minkowski functionals from the 512^3 section of the μ-CT image at resolution 8.06 μm are compared with the measurements from the corresponding 512^3 discretization of the model at the same resolution in Table II. As discussed earlier, ρ and $\lambda_{\max}$ are specifically calibrated to achieve as close a match as possible between the original rock and the modeled rock at this resolution. We claim that this will result in a realistic representation of the rock also at intermediate and higher resolutions.

TABLE II. Minkowski functionals computed from the digitized representations of the sample and the model at 8.06 μm resolution.

Sample resolution ($a=8.06$ μm)	Size M^3 (voxels)	Porosity $\phi=\phi_3$ (%)	Specific surface $\phi_2(\mathbb{P})$ (mm^{-1})	Mean curvature $\phi_1(\mathbb{P})$ (mm^{-2})	Total curvature $\phi_0(\mathbb{P})$ (mm^{-3})
μ-CT	512^3	29.4884	22.7875	354.054	31359.9
Model	512^3	28.9685	20.2673	297.341	31542.7

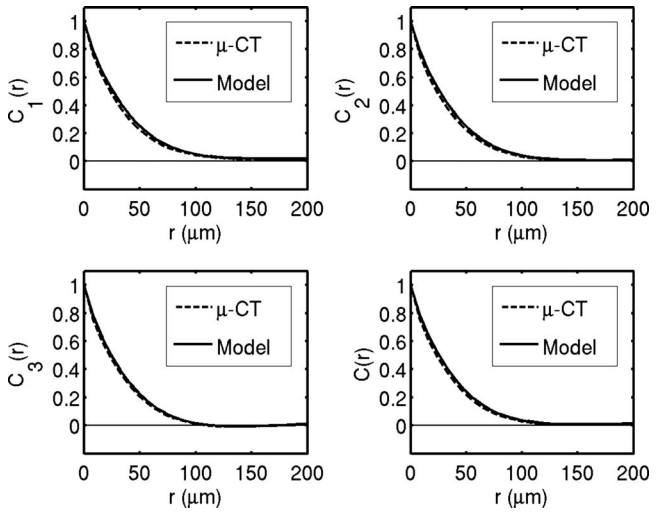

FIG. 7. Comparison of two-point correlation functions between the model and μ-CT image at 8.06 μm resolution. $C(r)$ is the average over all three directions.

B. Two-point correlation function

Further quantitative characterization and comparison of the microstructure is carried out through the two-point correlation function computed from the discretization of the model and the original μ-CT images at 8.06 μm. Assuming homogeneity, the directional two-point correlation functions $C_i(r)$ are defined as

$$C_i(r) = \frac{\langle [\chi_{\mathrm{P}}(\mathbf{x}) - \phi][\chi_{\mathrm{P}}(\mathbf{x} + r\mathbf{e}_i) - \phi] \rangle}{\langle [\chi_{\mathrm{P}}(\mathbf{x}) - \phi]^2 \rangle}, \tag{8}$$

where ϕ is the porosity of the sample and $i=1,2,3$. Their average is $C(r)=\Sigma_{i=1}^{3} C_i(r)$. The computed two-point correlation functions on the digitized representations of the model and μ-CT images at 8.06 μm resolution are plotted in Fig. 7. At this resolution, the model measurements agree reasonably well with that from the μ-CT image in all three directions. The slope of the tangent drawn at $C(0)$ provides a rough estimate of the specific surface area of the solid/void and is related to the permeability of the sample [2]. This suggests that along with the quantitative agreement in the porosities and in the morphologies (Table II), the transport properties computed from the model at this resolution are also expected to show reasonable agreement with those obtained from the experimental μ-CT image.

C. LPT measurements

A more detailed quantitative microstructure comparison is carried out using local porosity theory (LPT) [38,39]. The usefulness of this method has been established earlier in comparing μ-CT images of different sandstones [40] and comparing three-dimensional models of sandstones with the original [41]. In this method one measures geometric observables such as porosity or connectivity within a compact subset of the porous medium and collects these measurements into various histograms. For convenience of the reader we briefly repeat the basic definitions of the quantities used in LPT to characterize the porosity and connectivity fluctuations at different length scales in three-dimensional digitized models [2,42].

Within a cubic measurement cell $\mathbb{K}(\mathbf{r},L)$ of sidelength L centered at the lattice vector $\mathbf{r}$, the local porosity is defined as

$$\phi(\mathbf{r},L) = \frac{V[\mathbb{P} \cap \mathbb{K}(\mathbf{r},L)]}{V[\mathbb{K}(\mathbf{r},L)]}, \tag{9}$$

where $V[\mathbb{K}(\mathbf{r},L)]$ denotes the volume of a subset $\mathbb{K} \subset \mathbb{R}^3$. The *local porosity distribution* $\mu(\phi,L)$ is given by

$$\mu(\phi,L) = \frac{1}{m} \sum_{\mathbf{r}} \delta[\phi - \phi(\mathbf{r},L)], \tag{10}$$

where m is the number of placements of the measurement cell $\mathbb{K}(\mathbf{r},L)$ and $\delta[\phi-\phi(\mathbf{r},L)]$ is the Dirac delta function. For adequate statistics $\mathbb{K}(\mathbf{r},L)$ are placed on all lattice sites $\mathbf{r}$ which are at least a distance $L/2$ from the boundary of $\mathbb{S}$.

A measurement cell $\mathbb{K}(\mathbf{r},L)$ is *percolating in the* x (y,z) *direction* if there exists a connected path lying inside the pore space within the measurement cell between two points on the opposite boundary faces of $\mathbb{K}(\mathbf{r},L)$ perpendicular to the x (y,z) axis. The connectivity function is defined as

$$\Lambda_c(\mathbf{r},L) = \begin{cases} 1 & : \text{if } \mathbb{K}(\mathbf{r},L) \text{ percolates in } c \text{ direction} \\ 0 & : \text{otherwise.} \end{cases} \tag{11}$$

The function $\Lambda_c(\mathbf{r},L)$ is computed using the Hoshen-Kopelman algorithm [43]. The *local percolation probability* $\lambda_c(\phi,L)$ is defined through

$$\lambda_c(\phi,L) = \frac{\sum_{\mathbf{r}} \Lambda_c(\mathbf{r},L)\, \delta_{\phi\phi(\mathbf{r},L)}}{\sum_{\mathbf{r}} \delta_{\phi\phi(\mathbf{r},L)}}. \tag{12}$$

It gives the fraction of measurement cells of sidelength L with local porosity ϕ that are percolating in c direction. Here $\delta_{\phi\phi(\mathbf{r},L)}$ is the Kronecker delta. The *total fraction of percolating cells* of size L is given by the integration over all local porosities,

$$p_c(L) = \int_0^1 \mu(\phi,L)\lambda_c(\phi,L)d\phi. \tag{13}$$

The local percolation property is closely correlated with transport properties such as permeability or conductivity as was first pointed out in Ref. [41] and later verified in Ref. [26] for sandstones. LPT has also been used in Ref. [10] to analyze the percolation properties of low-porosity Fontainebleau sandstone.

LPT measurements are carried out on the three-dimensional (512^3) thresholded digitized image of the model and the μ-CT image at resolution 8.06 μm. In Fig. 8, $\mu(\phi,L)$ and $\lambda_3(\phi,L)$ are compared for three different values of L. At each of these measurement cell sizes the local porosity distribution and the local percolation probability (in all three directions) from the experimental image match with that from the model. Equally good agreement is observed

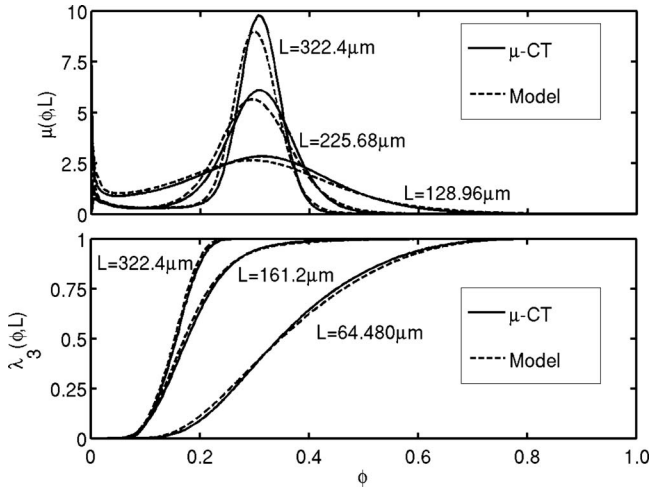

FIG. 8. Comparison of local porosity distribution and local percolation probabilities of the model and the μ-CT image at 8.06 μm.

between $p_c(L)$ plotted in Fig. 9. This suggests that at the resolution 8.06 μm, the pore scale microstructure of the modeled rock matches (quantitatively) very well with that of the experimental μ-CT image.

IX. PREDICTIONS AT HIGHER RESOLUTIONS

The quantitative comparison of the microstructure at the resolution 8.06 μm presented above establishes that the model discretization represents the original rock with significant accuracy at this level of resolution. The model, however, can now be discretized at any arbitrary resolution. The sample $\mathbb{S}$ is discretized at 16, 8, 4, 2, and 1 μm for predicting porosity and permeability at higher resolutions and to extrapolate to infinite resolution.

X-ray tomography of subsection plugs of diameters 3 and 1.5 mm was also carried out (ESRF, Grenoble, France) at higher resolutions, namely, 1.4 and 0.7 μm. The subsampling procedure is shown in Fig. 1. These higher resolution μ-CT images are from subregions different from the volume of the rock. The model is also discretized at resolutions 1.4 and 0.7 μm. In Fig. 10, cross sections from these synthetic μ-CT images from the model are compared with the experimental μ-CT images at the respective resolutions. An impressive visual match of the morphology is observed at these higher resolutions.

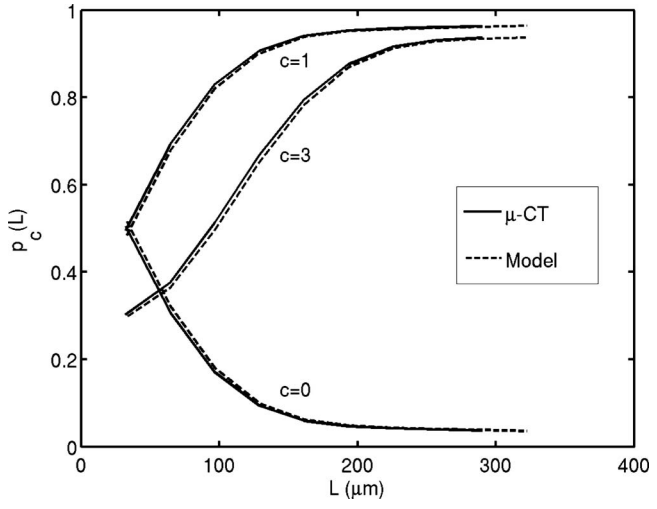

FIG. 9. Comparison of the fraction of percolating cells at different length scales for the model and the μ-CT image at 8.06 μm.

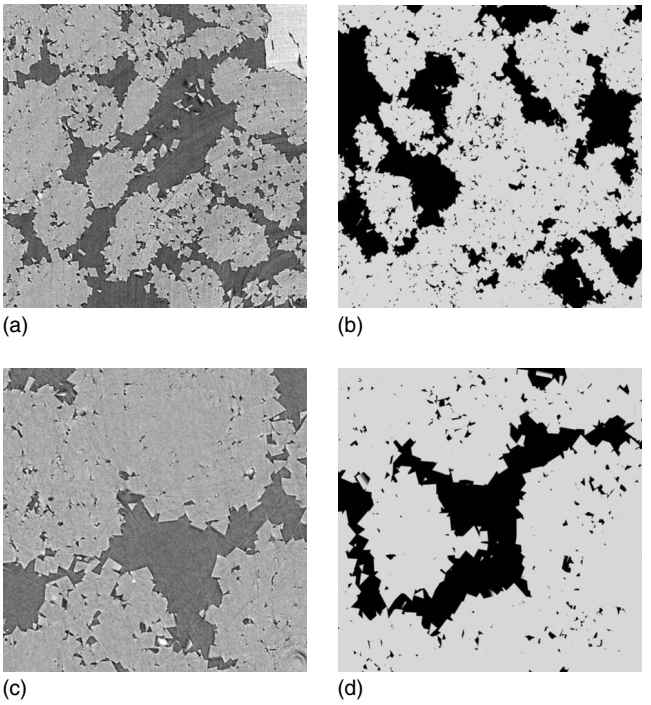

FIG. 10. Experimental μ-CT images of the carbonate rock (images on the left column) are compared with sections of the model discretization (synthetic μ-CT images from the model) at respective resolutions. Left (from top to bottom): 512×512 pixels experimental μ-CT images at resolution 1.4 μm and 0.7 μm, respectively. Right: 512×512 pixels subsections of corresponding model discretization showing the gradual resolution of the dolomites with higher resolution.

All measurements presented in this section are carried out on digitized representations of the experimental μ-CT images from the rock and the synthetic μ-CT images from the model. As mentioned before, the digitization is carried out by thresholding the discretizations (grayscale images) using the Otsu method [34].

The Minkowski functionals computed on all these samples are summarized in Tables II and III. For the higher resolution (1.4 and 0.7 μm) discretizations of the model, the Minkowski functionals are computed on two nonoverlapping subsamples (1000^3 voxels) selected randomly from the full sample discretization. Although the synthetic μ-CT images and the experimental μ-CT images correspond to different regions of the rock, the Minkowski functionals computed from the experimental μ-CT images and the model discretizations show reasonable agreement at the respective resolutions.

The computed porosities at increasing resolutions are plotted in Fig. 11. Although from different regions of the

TABLE III. Minkowski functionals computed from the binary images obtained by thresholding the experimental μ-CT images of the rock and the synthetic μ-CT images from the model at different resolutions. For the model discretizations at resolutions 1.4 and 0.7 μm, Minkowski functionals are computed from a pair each of nonoverlapping subsamples (1000^3 voxels) selected randomly.

Sample resolution a (μm)	Size M^3 (voxels)	Porosity $\phi=\phi_3$ (%)	Specific surface $\phi_2(\mathbb{P})$ (mm^{-1})	Mean curvature $\phi_1(\mathbb{P})$ (mm^{-2})	Total curvature $\phi_0(\mathbb{P})$ (mm^{-3})
Model					
16.0	256^3	28.8412	15.5884	106.124	−6911.31
8.0	512^3	29.0001	20.2203	303.091	33354.3
4.0	1024^3	29.4577	29.5054	1619.21	506456
2.0	2048^3	30.0681			
1.0	4096^3	30.6351			
1.4 (1)	1000^3	32.169	48.3124	6529.29	2.5×10^6
1.4 (2)	1000^3	29.412	48.2883	7095.59	2.59×10^6
0.7 (1)	1000^3	28.533	57.1416	10913.7	3.28×10^6
0.7 (2)	1000^3	27.475	53.7597	10105.9	3.03×10^6
μ-CT					
8.06	1000^3	30.5199	19.3285	131.688	−10358.8
1.4	1000^3	31.2905	63.4964	5109.51	271020
0.7 (1)	1000^3	32.3128	86.5955	8585.44	3.65×10^6
0.7 (2)	1000^3	32.9546	90.5366	12214.6	4.87×10^6

rock, the porosities of the experimental μ-CT images at higher resolutions are close to the value predicted by the model. For the model at resolutions of 16, 8, 4, 2, and 1 μm, the porosities are computed from the full sample discretizations. At 1.4 and 0.7 μm resolutions, the porosities are measured from subsamples of size 2048^3 voxels each. To assess the variations in the porosities in different regions, each of these volumes is divided into eight nonoverlapping subsamples and porosities are computed on each of them separately. The error bars shown at each resolution in Fig. 11 correspond to the variation in the computed porosities in these subsamples. For the real rock, the porosities are measured on μ-CT subsamples with 1000^3 voxels. The error bars show again the subsample variation in the porosities for these volumes. They are computed by subdividing these volumes into eight nonoverlapping subsamples. A close match of the porosity computed on the 512^3 voxel μ-CT subsample is achieved because the modeled region coincides with the region of the rock in the μ-CT image. The large variation in porosities in the subsamples is because the sizes of the experimental μ-CT images at higher resolutions (1.4 and 0.7 μm) are below REV scale (representative elementary volume scale at which the microstructure becomes homogeneous). Better resolution of the microporosity and internal surface is the primary reason behind the increase in porosity at higher resolutions. The original 3.81 cm diameter core plug was analyzed experimentally and had a He porosity of 30.1%. Incidentally, the extrapolated porosity for the fully resolved model (Fig. 11) is close to the experimental value for the full core plug.

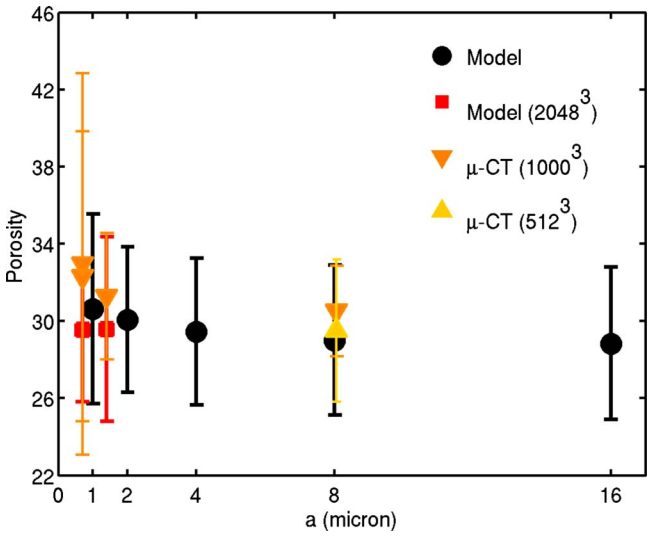

FIG. 11. (Color online) Porosities computed from synthetic μ-CT images of the model and from experimental μ-CT images at different resolutions. For the model, at resolutions 1.4 and 0.7 μm, the porosities are computed from a 2048^3 voxel subsample. Porosity denoted by μ-CT (512^3) at the resolution 8.06 μm is computed from the 512^3 subregion of the experimental μ-CT image from the rock that is used for constructing G. The error bars reflect the subsample variations in porosities computed by dividing each volume into eight nonoverlapping subvolumes.

The absolute permeability on these volumes is computed by solving the linear Stokes equation under incompressible flow condition using the public domain software "permsolver" [44]. The full model discretization at resolution 16 μm (256^3) is divided into eight subsamples of size 128^3 each. At resolution 8 μm (512^3) it is divided into eight subsamples of size 256^3 each, at resolution 4 μm (1024^3) it is divided into 64 subsamples of size 256^3 each, and at reso-

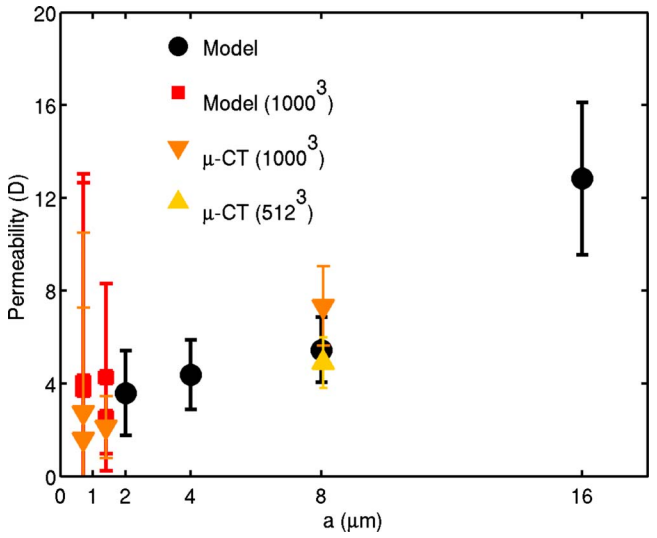

FIG. 12. (Color online) Absolute permeabilities computed from synthetic μ-CT images of the model and experimental μ-CT images from the rock at different resolutions. At resolutions 1.4 and 0.7 μm, the porosities are computed for 1000^3 voxel subsample discretizations from the model. The μ-CT (512^3) is the section of the rock at resolution 8.06 μm that is used for constructing G. The error bars reflect subsample variations.

lution 2 μm (2048^3) it is divided into 512 subsamples of size 256^3 each. At higher resolutions of 1.4 and 0.7 μm, a pair of nonoverlapping subsamples of size 1000^3 at each resolution is chosen randomly and further subdivided into 64 subsamples of size 250^3 each. The original μ-CT images of size 1000^3 at resolutions 8.06, 1.4, and 0.7 μm are also divided into 64 subsamples of size 250^3 each. The absolute permeabilities are measured on all of these subsamples. The average values along with subsample variation (error bars) for the model and the original rock at different resolutions are plotted in Fig. 12. The predictions from the model at intermediate and higher resolutions are remarkable as judged from the comparison with the computed permeabilities on the available μ-CT images. The large error bars at the higher resolutions of 1.4 and 0.7 μm arise because the subsample volumes are rather small and not representative. The permeability of the original core plug was experimentally measured as 1295 mD. The good agreement of the numerical result extrapolated to full resolution (Fig. 12) is likely coincidental because the model corresponds to a small subsection of the full core plug.

The changes in the petrophysical properties observed at higher resolutions are mainly due to the improved resolution of the microporosity. The thresholding procedure is also more accurate at higher resolutions. The property predictions can be more accurate if the model parameters are calibrated by matching the model discretization with the μ-CT images at more than one resolution. This, however, ideally requires that the higher resolution μ-CT images are from the same region and of the same volume of the modeled rock. In the proposed modeling method, the model parameters λ_{max} and ρ can be calibrated to increase or decrease the microporosity at higher resolutions without changing the macroporosity at lower resolutions.

X. SUMMARY AND DISCUSSION

We present an application of the continuum geometrical modeling technique proposed in Ref. [13] to predict transport properties of strongly correlated natural porous media. The approach comprises several modeling steps. Beginning with a subresolution μ-CT image of a carbonate rock and high-resolution two-dimensional images from the same rock, we reconstruct a pore scale representation of a large cubic volume of the rock at arbitrary resolution. The model parameters are then calibrated to quantitatively match the morphology of the low-resolution experimental μ-CT image with that of the synthetic μ-CT image from the model at the same resolution. The following geometric quantities are matched: the four Minkowski functionals, two-point correlation function, local porosity distributions, and local percolation probabilities. All the quantitative microstructure statistics are computed on binary representations of the μ-CT images obtained through an independent thresholding method. Although the quantitative morphology matching is done at a specific low resolution, the resulting model provides accurate predictions at higher resolutions for the carbonate rock modeled in this work.

We conclude that this modeling method is suitable to provide three-dimensional pore scale microstructures of laboratory scale carbonate rocks at arbitrary resolutions. Models of a full core plug, such as the one shown in the Fig. 1, can be generated with modest computational resources. We have generated a smaller size sample mainly because discretizations from such a sample size are feasible to analyze within the computational resources available to us currently. We showed that combining information from low-resolution μ-CT images and high-resolution two-dimensional images, fairly realistic models of multiscale porous media can be generated. Synthetic μ-CT images from the computational discretization of the model match well with the experimental μ-CT images at arbitrary resolutions. The method allows for a calibrated match of the microstructure and petrophysical transport properties at specific resolutions. It then provides reasonably accurate prediction of transport parameters at intermediate and higher resolutions where the microstructure is unknown. We hope that this method will find application in the investigation of three-dimensional pore scale microstructures in diverse scientific fields and will also lead to more accurate prediction of transport properties in multiscale porous media.

ACKNOWLEDGMENTS

The authors are grateful to StatoilHydro ASA, Norway for financial support and permission to publish this work. The authors further acknowledge Tony Boassen for providing SEM images and Sven Roth for processing the experimental μ-CT images of the rock. We thank the Scientific Supercomputing Center, Karlsruhe for providing the computing time and technical support.

APPENDIX: MINKOWSKI FUNCTIONALS

A geometric observable f is a mapping (functional) that assigns to each admissible pore space $\mathbb{P}$ a real number $f(\mathbb{P})$

$=f(\mathbb{P}\cap\mathbb{S})$ that can be calculated from $\mathbb{P}$ without solving a physical boundary value problem. The set $\mathcal{R}$ of admissible $\mathbb{P}$ is defined as the set of all finite unions of compact convex sets [30,45]. The set of all compact and convex subsets of $\mathbb{R}^d$ is denoted as $\mathcal{K}$. Examples of geometric observables are the volume of $\mathbb{P}$ or the surface area of the internal $\partial\mathbb{P}=\partial\mathbb{M}=\mathbb{P}\cap\mathbb{M}$. Let

$$V_d(\mathbb{K}) = \int_{\mathbb{R}^d} \chi_{\mathbb{P}}(\mathbf{r}) d^d\mathbf{r} \tag{A1}$$

denote the d-dimensional Lebesgue volume of the compact convex set $\mathbb{K}$. The volume is hence a functional $V_d:\mathcal{K}\to\mathbb{R}$ on $\mathcal{K}$. An example of a compact convex set is the unit ball $\mathbb{B}^d=\{\mathbf{x}\in\mathbb{R}^d:|\mathbf{x}|\le 1\}=\mathbb{B}^d(\mathbf{0},1)$ centered at the origin $\mathbf{0}$ whose volume is

$$\kappa_d = V_d(\mathbb{B}^d) = \frac{\pi^{d/2}}{\Gamma[1+(d/2)]}. \tag{A2}$$

Other functionals on $\mathcal{K}$ can be constructed from the volume by virtue of the following fact. For every compact convex $\mathbb{K}\in\mathcal{K}$ and every $\varepsilon\ge 0$ there are numbers $V_j(\mathbb{K})$, $j=0,\ldots,d$ depending only on $\mathbb{K}$ such that

$$V_d(\mathbb{K}+\varepsilon\mathbb{B}^d) = \sum_{j=0}^{d} V_j(\mathbb{K})\varepsilon^{d-j}\kappa_{d-j} \tag{A3}$$

is a polynomial in ε. This result is known as Steiners formula [30,45]. The numbers $V_j(\mathbb{K})$, $j=0,\ldots,d$ define functionals on $\mathcal{K}$ similar to the volume $V_d(\mathbb{K})$. The quantities

$$W_i(\mathbb{K}) = \frac{\kappa_i V_{d-i}(\mathbb{K})}{\binom{d}{i}} \tag{A4}$$

are called quermassintegrals [46]. From Eq. (A3) one sees that

$$\lim_{\varepsilon\to 0}\frac{1}{\varepsilon}[V_d(\mathbb{K}+\varepsilon\mathbb{B}^d)-V_d(\mathbb{K})] = \kappa_1 V_{d-1}(\mathbb{K}), \tag{A5}$$

and from Eq. (A2) that $\kappa_1=2$. Hence, $V_{d-1}(\mathbb{K})$ may be viewed as half the surface area. The functional $V_1(\mathbb{K})$ is related to the mean width $w(\mathbb{K})$ defined as the mean value of the distance between a pair of parallel support planes of $\mathbb{K}$. The relation is

$$V_1(\mathbb{K}) = \frac{d\kappa_d}{2\kappa_{d-1}} w(\mathbb{K}), \tag{A6}$$

which reduces to $V_1(\mathbb{K})=w(\mathbb{K})/2$ for $d=3$. Finally the functional $V_0(\mathbb{K})$ is evaluated from Eq. (A3) by dividing with ε^d and taking the limit $\varepsilon\to\infty$. It follows that $V_0(\mathbb{K})=1$ for all $\mathbb{K}\in\mathcal{K}\backslash\{\emptyset\}$. One extends V_0 to all of $\mathcal{K}$ by defining $V_0(\emptyset)=0$. The geometric observable V_0 is called Euler characteristic.

For a three-dimensional porous sample with $\mathbb{P}\in\mathcal{R}$ the extended functionals V_i lead to the geometric observables known as Minkowski functionals. The first is the porosity of a porous sample $\mathbb{S}$ defined as

$$\phi(\mathbb{P}\cap\mathbb{S}) = \phi_3(\mathbb{P}\cap\mathbb{S}) = \frac{V_3(\mathbb{P}\cap\mathbb{S})}{V_3(\mathbb{S})} \tag{A7}$$

and the second is its specific internal surface area which may be defined in view of Eq. (A5) as

$$\phi_2(\mathbb{P}\cap\mathbb{S}) = \frac{2V_2(\mathbb{P}\cap\mathbb{S})}{V_3(\mathbb{S})}. \tag{A8}$$

The two remaining observables, the mean curvature $\phi_1(\mathbb{P}\cap\mathbb{S})=V_1(\mathbb{P}\cap\mathbb{S})/V_3(\mathbb{S})$ and the total curvature $\phi_0(\mathbb{P}\cap\mathbb{S})=V_0(\mathbb{P}\cap\mathbb{S})/V_3(\mathbb{S})$, have received less attention in the porous media literature.

[1] M. Sahimi, Rev. Mod. Phys. **65**, 1393 (1993).
[2] R. Hilfer, Adv. Chem. Phys. **92**, 299 (1996).
[3] J. B. Maillet and P. V. Coveney, Phys. Rev. E **62**, 2898 (2000).
[4] R. Hilfer and C. Manwart, Phys. Rev. E **64**, 021304 (2001).
[5] I. I. Bogdanov, V. V. Mourzenko, J. F. Thovert, and P. M. Adler, Phys. Rev. E **68**, 026703 (2003).
[6] G. Jin, T. W. Patzek, and D. B. Silin, SPE Tech. Report No. 90084, 2004 (unpublished).
[7] K. Wu, M. Van Dijke, G. Couples, Z. Jiang, J. Ma, K. Sorbie, J. Crawford, I. Young, and X. Zhang, Transp. Porous Media **65**, 443 (2006).
[8] P. M. Adler, *Porous Media—Geometry and Transports* (Butterworth-Heinemann, Boston, 1992).
[9] C. L. Y. Yeong and S. Torquato, Phys. Rev. E **57**, 495 (1998).
[10] J.-F. Thovert, F. Yousefian, P. Spanne, C. G. Jacquin, and P. M. Adler, Phys. Rev. E **63**, 061307 (2001).
[11] C. H. Arns, M. A. Knackstedt, and K. R. Mecke, Phys. Rev. Lett. **91**, 215506 (2003).
[12] R. Hilfer and B. Biswal, STATOIL Technical Report No. 4500523922, 2006 (unpublished).
[13] B. Biswal, P. E. Øren, R. J. Held, S. Bakke, and R. Hilfer, Phys. Rev. E **75**, 061303 (2007).
[14] A. P. Roberts, Phys. Rev. E **56**, 3203 (1997).
[15] M. G. Rozman and M. Utz, Phys. Rev. E **63**, 066701 (2001).
[16] M. G. Rozman and M. Utz, Phys. Rev. Lett. **89**, 135501 (2002).
[17] H. Okabe and M. J. Blunt, Phys. Rev. E **70**, 066135 (2004).
[18] P. M. Adler, C. G. Jacquin, and J. A. Quiblier, Int. J. Multiph. Flow **16**, 691 (1990).
[19] P. M. Adler, C. G. Jacquin, and J. F. Thovert, Water Resour. Res. **28**, 1571 (1992).
[20] A. P. Roberts and M. Teubner, Phys. Rev. E **51**, 4141 (1995).
[21] C. L. Y. Yeong and S. Torquato, Phys. Rev. E **58**, 224 (1998).
[22] C. Manwart, S. Torquato, and R. Hilfer, Phys. Rev. E **62**, 893 (2000).
[23] S. Bakke and P. E. Øren, SPE J. **2**, 136 (1997).

[24] P. E. Øren and S. Bakke, Transp. Porous Media **46**, 311 (2002).
[25] G. Jin, T. W. Patzek, and D. B. Silin, SPE Tech. Report No. 83587, 2003 (unpublished).
[26] C. Manwart, U. Aaltosalmi, A. Koponen, R. Hilfer, and J. Timonen, Phys. Rev. E **66**, 016702 (2002).
[27] M. Knackstedt *et al.*, Proceedings of the International Symposium of the Society of Core Analysts (unpublished).
[28] S. Youssef, M. Han, D. Bauer, E. Rosenberg, S. Bekri, M. Fleury, and O. Vizika, Proceedings of the International Symposium of the Society of Core Analysts (unpublished).
[29] R. Dunham, in *Classification of Carbonate Rocks: American Association of Petroleum Geologists*, edited by W. Ham (American Association of Petroleum Geologists, Tulsa, OK, 1962), pp. 108–121.
[30] D. Stoyan, W. S. Kendall, and J. Mecke, *Stochastic Geometry and Its Applications* (Wiley-VCH, New York, 1995).
[31] C. H. Moore, *Carbonate Diagenesis and Porosity* (Elsevier, Amsterdam, 1989).
[32] W. S. Rasband, IMAGEJ, U.S. National Institutes of Health, Bethesda, Maryland, USA, http://rsb.info.nih.gov/ij/ (1997–2008).
[33] M. D. Abramoff, P. J. Magelhaes, and S. J. Ram, Biophotonics Int. **11**, 36 (2004).
[34] P. K. Sahoo, S. Soltani, and K. C. Wong, Comput. Vis. Graph. Image Process. **41**, 233 (1988).
[35] F. N. Rhines, *Microstructology: Behavior and Microstructure of Materials* (Dr. Riederer-Verlag GmbH, Germany, 1986).
[36] J. Ohser and F. Mücklich, *Statistical Analysis of Microstructures in Material Science: Statistics in Practice* (John Wiley & Sons, New York, 2000).
[37] C. Lang, J. Ohser, and R. Hilfer, J. Microsc. **203**, 303 (2001).
[38] R. Hilfer, Phys. Rev. B **44**, 60 (1991).
[39] R. Hilfer, Phys. Rev. B **45**, 7115 (1992).
[40] B. Biswal, C. Manwart, and R. Hilfer, Physica A **255**, 221 (1998).
[41] B. Biswal, C. Manwart, R. Hilfer, S. Bakke, and P. E. Øren, Physica A **273**, 452 (1999).
[42] R. Hilfer, Transp. Porous Media **46**, 373 (2002).
[43] D. Stauffer and A. Aharony, *Introduction to Percolation Theory* (Taylor and Francis, London, 1992).
[44] D. P. Bentz and N. S. Martys, NIST Internal Report, NISTIR Tech. Report No. 7416, 2007 (unpublished); ftp://ftp.nist.gov/pub/bfrl/bentz/permsolver/
[45] H. Hadwiger, *Altes und Neues über Konvexe Körper* (Birkhäuser, Basel, 1955).
[46] R. Schneider, *Convex Bodies: The Brunn-Minkowski Theory* (Cambridge University Press, Cambridge, 1993).